DOI: 10.61782/fa.2023.1300

forum acusticum 2023

# DYNAMICS OF AN ACOUSTIC TEMPORAL METAGRATING

**Massimo Ruzzene**
Dept. of Mechanical Engineering
University of Colorado Boulder, USA
massimo.ruzzene@colorado.edu

**Emanuele Riva**
Dept. of Mechanical Engineering
Politecnico di Milano, Italy
emanuele.riva@polimi.it

**Matheus Rosa**
Dept. of Mechanical Engineering
University of Colorado Boulder, USA
matheus.rosa@colorado.edu

## ABSTRACT

This talk describes analytical, numerical, and experimental studies on an acoustic temporal metagrating. The concept of a space metagrating – a metamaterial whose resonating units are smoothly varied in space - has been long studied and its features are now well-established. A spatial variation of resonances leads to effects such as rainbow trapping and spatial signal compression, which are related to a gradual spatial wavenumber variation occurring at fixed temporal frequencies. We introduce the temporal analogue of such gratings and explore the resulting wave phenomena emerging by virtue of time modulation. The implementation, based on an acoustic waveguide endowed with tunable Helmholtz resonators, leverages the synergistic interplay between local resonance and time modulation, and offers exquisite control of the underlying dispersion properties. Numerical simulations and experimental studies unveil a few functionalities inherently present in such a system when the properties of the resonators are gradually varied over time. In analogy with space metagratings, we demonstrate frequency conversion, and the temporal rainbow effect, which are suitable to produce fast-and-compressed or slow-and-dilated versions of impinging temporal signals. The framework presented herein may open new avenues in the context of time-varying phononics, with applications to communication, sound isolation, and energy conversion.

**Keywords:** *Acoustic metamaterials, time compression, time-varying resonances.*

**Corresponding author*: massimo.ruzzene@colorado.edu.


## 1. INTRODUCTION

The metamaterials research has investigated intriguing phenomena to functionally control wave propagation within different physical domains. Various implementations in optical, elastic, and acoustic systems showcase examples produced by periodic tessellations of Bragg-scattering or locally-resonant units, which define different bandgap formation mechanisms responsible for the ensuing wave propagation features [1]. A number of wave manipulation strategies have emerged to provide attenuation [2], localization [3], and mode-conversion [4] capabilities in acoustics, which are of particular relevance for sound and vibration isolation purposes. Other configurations rely on the careful manipulation of spatial symmetries in the creation of back-scattering immune topological waveguides [5], including elastic/acoustic analogs to the quantum spin Hall (QSH) [6] and quantum valley Hall (QVH) [7] effects, for example. Another line of work takes advantage of metamaterials with gradually varying units, which are known to support slow waves [8] produced by way of a gradual decrease of the wave's speed in space, and which may also be useful for practical applications such as energy harvesting [9] and enhanced sensing [10]. All these examples are induced by a modulation of the underlying media in space. However, wave propagation in spatially periodic or spatially varying systems is constrained by non-tuneable dispersion and frequency-invariant characteristics, which dictate severe limitations on the achievable dynamics. Time-modulated metamaterials are excellent candidates to overcome these limitations and broaden the wave control opportunities in the context of metamaterial-based waveguiding. For instance, nonreciprocal wave propagation [11], temporal pumping [12], and temporal waveguiding [13] are behaviors that cannot be met by solely linear time-invariant interactions. In this context, we study wave propagation in time-modulated

acoustic metamaterials in light of the adiabatic theorem. Our analysis is inspired by previous studies on adiabatic transformations of standing modes [14], and on adiabatic wave steering in spring-mass lattices [15]. Here, we explore an acoustic waveguide endowed with Helmholtz resonators, where the cross-section of the neck is modulated in time. We show that an incident wave packet propagating through the time-varying waveguide undergoes a wavenumber-invariant frequency conversion that follows the time evolution of the dispersion bands. The role of the modulation velocity is explored through the adiabatic theorem. We show that quick (non-adiabatic) modulation protocols generate energy leaks from the incident wave packet toward other wave modes that populate the waveguide. We then compute a limiting condition for the modulation velocity in order to achieve frequency conversion through a scattering-free process and delineate the transition between adiabatic and non-adiabatic processes. Supported by the derived adiabatic conditions, our numerical results reveal possibilities for frequency conversion and temporal signal compression or decompression, which may define novel functionalities of metamaterial waveguides enabled by smooth temporal modulations.

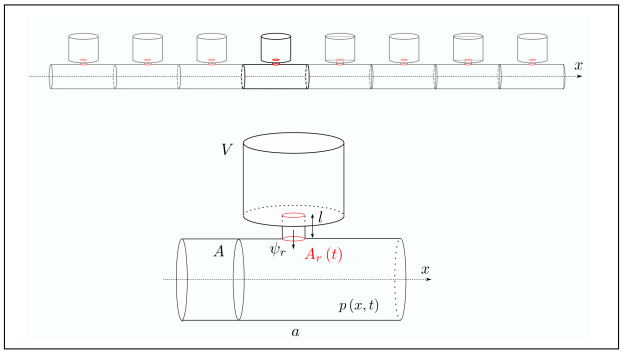


**Figure 1**. Schematic of the waveguide endowed with Helmholtz resonators, along with a zoomed view of the unit cell. The neck cross-section area $A_r$, highlighted in red, is modulated in time, while the other parameters are kept constant.

## 2. ACOUSTIC WAVEGUIDES WITH TIME-VARYING RESONATORS: MODELING AND SOLUTION METHODS

In this section, we describe the modeling of the one-dimensional (1D) acoustic waveguide endowed with time-varying Helmholtz resonators. We first derive the equations of motion of the coupled system, followed by a homogenization in the long-wavelength limit which allows for analytical expressions of the dispersion relations in the absence of time modulation. Finally, we describe the adiabatic conditions for transformations induced by slow time modulation of the resonators' properties, which delineates the transition between frequency conversion with and without energy scattering toward undesired wave modes.

### 2.1 Equations of motion

We consider a 1D acoustic waveguide of constant cross-section area $A$, featuring a period array of Helmholtz resonators of volume $V$, spaced by a distance $a$ (Fig. 1). The resonators have a neck length $l$ and neck area $A_r(t)$, the latter assumed to be mechanically varied in time. The wave equation for the acoustic waveguide is expressed as [16]:

$$\frac{1}{c^2}\frac{\partial^2 p}{\partial t^2} - \frac{\partial^2 p}{\partial x^2} = \frac{\partial G}{\partial t} \tag{1}$$

where $p = p(x,t)$ is the pressure field along the pipe, $c$ is the speed of sound, and $G(x,t)$ is the apparent rate of input mass per unit volume associated with the resonators. We assume a lumped-parameter model for the resonators, whose only degree of freedom $\psi(t)$ is the outward fluid displacement of the neck, which is constant along the cross-sectional area $A_r$. Under this approximation, the resonators are tuned to a frequency $\omega_r(t) = c\sqrt{A_r(t)/Vl'}$ which also varies in time, with $l' = l + 1.7r$ being the effective neck length of a flanged resonator whose cylindrical neck has a radius $r$ [16]. The apparent input mass rate provided by a single resonator is given by $g = \rho A_r(t)\partial\psi/\partial t$, where $\rho$ is the air density. Therefore, the expression for the total rate per unit volume accounting for a series of $N$ resonators is expressed as:

$$G(x,t) = \sum_{j=1}^{N} \rho \frac{A_r}{A}\frac{\partial \psi_j}{\partial t}\delta(x - x_j), \tag{2}$$

where $\delta(x - x_j)$ is the delta function that accounts for the assumed point-wise action of the $j_{th}$ resonator placed at $x_j$. Substitution of 3 into 1 yields the equations of motion

of the waveguide coupled with those of the resonators:

$$\frac{1}{c^2}\frac{\partial^2 p}{\partial t^2} - \frac{\partial^2 p}{\partial x^2} = \rho \sum_{j=1}^{N} \left( \frac{A_r}{A}\frac{\partial^2 \psi_j}{\partial t^2} + \frac{1}{A}\frac{\partial A_r}{\partial t}\frac{\partial \psi_j}{\partial t} \right) \delta\left(x - x_j\right)$$
$$m\frac{\partial \psi_j^2}{\partial t^2} + \frac{\partial m}{\partial t}\frac{\partial \psi_j}{\partial t} + k\psi_j = -A_r p(x_j), \qquad j = 1, 2, ..., N \tag{3}$$

where $m = \rho A_r l'$ and $k = \rho c^2 A_r^2 / V$ are the effective mass and stiffness parameters of the resonators [16].

### 2.2 Dispersion calculation in the subwavelength regime

In order to investigate wave motion in the considered system and carry out analytical derivations, we now consider the homogenized version of Eq. 3, whereby the resonators are continuously distributed through the pipe:

$$\frac{1}{c^2}\frac{\partial^2 p}{\partial t^2} - \frac{\partial^2 p}{\partial x^2} = \frac{\rho}{a}\left( \frac{A_r}{A}\frac{\partial^2 \psi}{\partial t^2} + \frac{1}{A}\frac{\partial A_r}{\partial t}\frac{\partial \psi}{\partial t} \right)$$
$$m\frac{\partial \psi^2}{\partial t^2} + \frac{\partial m}{\partial t}\frac{\partial \psi}{\partial t} + k\psi = -A_r p. \tag{4}$$

Here, both $p\left(x,t\right)$ and $\psi\left(x,t\right)$ are continuous functions of space and time. This approximation is accurate in the subwavelength regime, i.e. when the lattice size is much smaller than the wavelength ($a << \lambda$), and therefore there is a sufficiently dense distribution of resonators compared to the wavelength at the operating frequency. Equation 4 is generally dependent upon the instantaneous value $A_r(t)$, and the rates $\partial A_r/\partial t$ and $\partial m/\partial t$. We first evaluate the dispersion in the time-invariant regime, i.e. assuming $\partial A_r/\partial t = 0$ and $\partial m/\partial t = 0$, with the area $A_r$ considered as a free parameter. The obtained solutions form the basis for the adiabatic expansion under smooth temporal modulations derived in the next section. Therefore, we seek a plane wave solution of the form $p\left(x,t\right) = p_0 \mathrm{e}^{\mathrm{i}(\kappa x - \omega t)}$ and $\psi\left(x,t\right) = \psi_0 \mathrm{e}^{\mathrm{i}(\kappa x - \omega t)}$, where $\omega$ and $\kappa$ are respectively angular frequency and wavenumber. Substitution into Eq. 4 yields the following dispersion relation:

$$\kappa = \pm\frac{\omega}{c}\sqrt{1 + \frac{\mu}{1 - \frac{\omega^2}{\omega_r^2}}} \tag{5}$$

where $\mu = V/aA$ is the volume ratio, i.e. the ratio between the volume enclosed in the resonator's chamber and the volume of the unit cell's pipe segment.

The dispersion relation $\omega\left(\kappa\right)$ is illustrated in Fig. 2 for two distinct conditions of $A_r$, corresponding to the initial and final modulation values $A_r^{(i)} = 10^{-5}\mathrm{mm}^2$ (solid line) and $A_r^{(f)} = 5 \cdot 10^{-5}\mathrm{mm}^2$ (dotted line) employed in the numerical part of the paper. Other relevant parameters of the resonator are $a = 16$ mm $l = 4$ mm, and $r = 8$ $mm$. In the figure, dimensionless frequencies $\Omega = \omega a/\pi c$ highlight the subwavelength operational regime ($\Omega < 0.5$). Only two dispersion branches with positive frequencies $\Omega_1$ and $\Omega_2$ are shown in the figure, which define waves propagating to the right. The dispersion is symmetric about the wavenumber axis, with the two leftward propagating solutions $\Omega_{-2} = -\Omega_2$ and $\Omega_{-1} = -\Omega_1$ not shown in the figure for ease of visualization. The presence of the Helmholtz resonators breaks the typical linear dispersion curve of the pipe into two dispersion bands separated by a bandgap, whose bounds can be easily extracted from the analytical solutions. The lower bound $\omega_l = \omega_r$ takes the wavenumber $\kappa$ to infinity in Eq. 6, while the upper bound is estimated as $\omega_u = \omega_r\sqrt{1+\mu}$. We observe that the relative gap width $\Delta\omega/\omega_r = (\omega_u - \omega_l)/\omega_r = \sqrt{1+\mu} - 1$ is determined solely by the resonator volume ratio $\mu$, which plays a similar role to the mass ratio of mechanical resonators [17]. The examples in Fig. 2 employ a fixed volume ratio of $\mu = 0.66$, and normalized tuning frequencies of $\Omega_r = 0.127$ and $\Omega_r = 0.23$ induced by the initial $A_r^{(i)}$ and final $A_r^{(f)}$ modulation values, respectively (note that the neck area does not influence the volume ratio $\mu$). The validity of the analysis in the subwavelength regime is confirmed by comparison with numerical simulations in Sec. 3 that consider Eq. 3 without the subwavelength approximation.

While here the area $A_r\left(t\right)$ is treated as a free parameter, its temporal variation modifies the dispersion properties of the pipe during wave propagation, producing a transformation that preserves the wavenumber content while promoting conversions of the frequency content across the modulation [18]. We seek an adiabatic transformation represented with the black vertical arrow, whereby the energy initially injected in $\Omega_1^{(i)}\left(\kappa^*\right)$ follows the time evolution of the underlying dispersion until the value $A_r\left(t\right)$ reaches $A_r^{(f)}$, without triggering any energy conversion to other wave modes. In contrast, nonadiabatic transformations triggered by fast modulation protocols induce energy scattering to the neighboring wave modes that populate the dispersion at different frequencies $\Omega_j\left(\kappa^*\right)$. In the following, we characterize these transformations in

the light of the adiabatic theorem, which allows us to delineate the transition between waveguiding with and without scattering in time-varying acoustics.

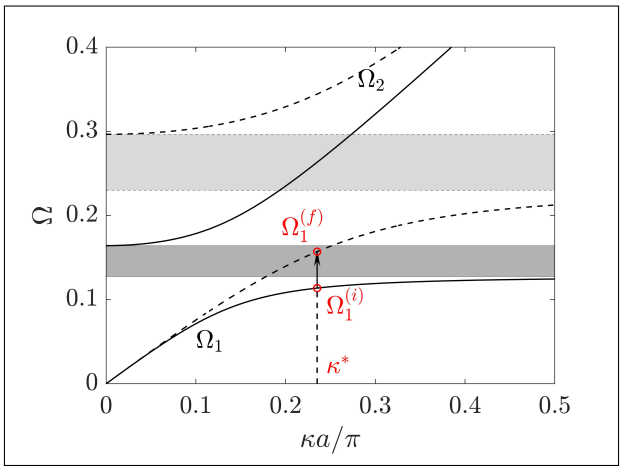


**Figure 2**. Dispersion relation before (solid line) and after (dashed line) time-modulation. The gray boxes highlight the corresponding variation of the gap limits. The energy, provided with a central frequency $\Omega_1^i$ and wavenumber $\kappa^*$, undergoes an adiabatic transformation that follows the vertical arrow and is accompanied by frequency conversion from $\Omega_1^i$ to $\Omega_1^f$. In contrast, nonadiabatic processes involve also other dispersion branches.

### 2.3 Adiabatic transformations for slow temporal modulations

To investigate the time-varying dynamics caused by slow temporal variations of the area $A_r$, Eq. 4 is written in a first-order differential form by imposing only the wavenumber $\kappa$:

$$|\hat{z}_{,t}\rangle = H\left(\kappa, A_r\left(t\right)\right)|\hat{z}\rangle \tag{6}$$

where $|\hat{z}\rangle = [\frac{\partial\hat{p}}{\partial t}, \frac{\partial\hat{\psi}}{\partial t}, \hat{p}, \hat{\psi}]^T$, also $,t$ denotes a temporal derivative and $H\left(\kappa, A_r\left(t\right)\right)$ is the time-dependent Hamiltonian matrix.

This first-order differential form resembles Schrodinger's equations for quantum states where the adiabatic theorem is classically established (see for example the book by [19]), and also employed in multiple following studies due to its convenience in deriving adiabatic conditions [20, 21]. The ansatz $|\hat{z}\rangle = |\hat{z}_0\rangle\, \mathrm{e}^{\mathrm{i}\omega t}$ yields a time-dependent eigenvalue problem of the form $H\left(\kappa, A_r\left(t\right)\right)|\hat{z}_j^R\rangle = \mathrm{i}\omega_\mathrm{j}|\hat{z}_j^R\rangle$, whose instantaneous solutions define the time-varying dispersion branches $\omega_j(\kappa, t)$ and associated eigenvectors $|\hat{z}\rangle^R(\kappa, t)$. In the case of smooth modulations produced by small rates of change of the area $A_r(t)$, the instantaneous dispersion solutions define the four time-dependent waves that can propagate in the pipe, and form a natural basis for the expansion of the total solution:

$$|\hat{z}\rangle(t) = \sum_j c_j(t)|\hat{z}_j^R\rangle(t)\mathrm{e}^{\mathrm{i}\theta_j}, \qquad j = [-2, -1, 1, 2], \tag{7}$$

where $\theta_j = \int_0^t \omega_j\left(\tau\right) d\tau$ is the geometric phase, which replaces the $\omega t$ term commonly present in time-independent solutions, and $c_j(t)$ are the time-dependent participation factors for each wave mode. Plugging the solution into Eq. 6 and performing a series of algebraic manipulations [15] yields the following differential equation that describes the time evolution of the participation factor $c_r(t)$:

$$c_{r\,,t} = -\langle\hat{z}_r^L|\hat{z}_{r,\,t}^R\rangle\; c_r - \sum_{j\neq r}\frac{\langle\hat{z}_r^L|H_{\,,t}|\hat{z}_j^R\rangle}{\mathrm{i}\left(\omega_j - \omega_r\right)} c_j \mathrm{e}^{\mathrm{i}(\theta_j - \theta_r)}, \tag{8}$$

where $\langle z_r^L|(t)$ is the left eigenvector. For a given initial condition defined by a combination of propagating modes, these equations can be solved to obtain the time evolution of each participation factor $c_r(t)$. While that is not always convenient, the equations are particularly useful to derive the conditions for adiabatic transformations in which the evolution occurs through an isolated mode. This leads to the following condition [22]:

$$\left|\frac{\langle\hat{z}_j^L\,|H_{\,,t}|\,\hat{z}_r^R\rangle}{\left(\omega_h - \omega_r\right)^2}\right| << 1. \tag{9}$$

The condition in Eq. 9 is employed to analyze the coupling between the imposed wave mode and the other modes which may be involved in the solution. The condition must be evaluated for a given pair of wave modes and a certain imposed wavenumber. To exemplify, we consider the imposed wavenumber $k^*$ and solution $\Omega_1$ marked in Fig. 2.

## 3. NUMERICAL RESULTS

In this section, we present a few case studies to elucidate the role of time modulation in the considered acous-

tic metamaterials, with emphasis on frequency conversion, mode conversion, and the derived adiabatic conditions. The results are obtained through numerical simulations performed through a finite difference time domain (FDTD) algorithm, where the partial derivatives in Eq. 3 are discretized through a central difference approximation. For simplicity, we employ a piecewise linear variation of the neck cross-section area:

$$A_r(t) = \begin{cases} A_r^{(i)} & t < t_i \\ A_r^{(i)} + v_m(t - t_i) & t_i < t < t_f \\ A_r^{(f)} & t > t_f \end{cases} \quad (10)$$

where $t_i$ and $t_f$ are the start and finish time instants for the modulation, and $v_m$ is the constant modulation velocity. In the simulations, a sinusoidal wave packet with $n = 30$ periods is imposed through a prescribed velocity to the left end of the waveguide. The excitation occurs during the time-invariant window $t < t_i$, establishing a propagating wave packet with a desired frequency/wavenumber spectral content according to the dispersion at the initial state $A_r = A_r^{(i)}$. We hereafter present the following representative examples: (i) a fast (nonadiabatic) modulation with $v_m = v_m^{(1)}$, which allows increasing the frequency content of an impinging wave packet while compressing its time envelope. Such a nonadiabatic process is accompanied by energy leakage toward the other states supported by the waveguide, (ii) a slow (adiabatic) modulation with $v_m = v_m^{(2)}$ able to perform frequency up-conversion and compression of an impinging wave packet, but without any energy leakage toward other wave modes, and (iii) an adiabatic frequency down-conversion with $v_m = v_m^{(2)}$, which is accompanied by dilation of the impinging wave packet, i.e., the process opposite to (ii).

The time history relative to example (i) is displayed in Fig. 3(a). The excitation is provided with a central frequency $\Omega_1^{(i)} = \Omega_1(\kappa^*) = 0.109$, targeting the lower dispersion branch of Fig. 2(a) in the nearly-flat region close to the resonance, which exhibits limited group velocity and highly dispersive characteristics. This region is chosen as it exhibits a large change with respect to the final dispersion branch (dashed lines in Fig. 2(a)) for the imposed wavenumber. In this example, the modulation takes place in a nonadiabatic manner due to the high modulation speed $v_m^{(1)}$, and the energy content is leaked to other available states supported by the waveguide. Indeed, wave motion in Fig. 3(a) exhibits sharp changes after time modulation, with distinct wave packets of different amplitude and speeds emerging. To better elucidate this concept, we report the wave packets before (black curves) and after (red curves) time modulation. Fig. 3(b) illustrates the spatial envelope of the wave and its wavenumber content, evaluated at fixed time instants (marked with dots in Fig. 3(a)). We note that, as expected of temporal modulations and discontinuities [13], the wavelength and associated wavenumber content are preserved throughout the process. In contrast, the corresponding frequency content undergoes transformations, as illustrated in Fig. 3(c) which displays the time and frequency representation of the wave packet for fixed spatial positions before and after time modulation. We note that the main frequency component of the wave packet undergoes a frequency shift toward a higher frequency $\Omega_1^{(f)}$, and its spectral width broadens after time modulation, which corresponds to a compression of the time-domain signal. An additional frequency component centered at $\Omega_2^{(f)}$ is also noted after the time modulation due to the scattering caused by the non-adiabatic process.

To better illustrate the frequency transformations, we present a frequency spectrogram in Fig. 3(d), which is evaluated by windowing the pressure field $p(x,t)$ with a moving Gaussian function $G(t) = \mathrm{e}^{-(t-t_0)^2/2c_0^2}$. Here, $c_0 = 0.06T_f$ determines the width of the Gaussian and $t_0$ is its central value, which is smoothly varied to produce the spectrogram within the interval $t_0 \in [0, t_f]$. For ease of visualization, the Fourier-transformed pressure field $\hat{p}(\kappa, f, t_0)$ is further processed by taking the RMS value along $\kappa$, which eliminates one dimension. The resulting spectrogram $|\hat{p}(f, t_0)|$ in Fig. 3(d) is overlaid to black curves that represent the wave modes $\Omega_j(\kappa^*)$ supported by the waveguide at the incident wavenumber $\kappa^*$. As expected, the energy content is initially concentrated in the branch $\Omega_1^{(i)}$, and its mainly converted through the evolution of that branch to $\Omega_1^{(f)}$. Due to the non-adiabatic transformation, other wave modes are present after modulation: the second branch $\Omega_2^{(f)}$ significantly contributes to the wave motion, and minor contributions are also observed for $\Omega_{-1}^{(f)}$ and $\Omega_{-2}^{(f)}$, generating back-propagating waves. Note that around $t = 30$ ms the back-propagating waves are reflected off the left boundary and converted back into the right propagating modes $\Omega_1$ and $\Omega_2$. Finally, Figs. 3(e-f) display the 2D Fourier Transforms of the pressure field before and after time modulation, overlaid to the numerical dispersion curves for the initial and final states. These diagrams confirm that frequency conversion follows the

underlying dispersion, with energy initially concentrated in the excited first branch, and afterward leaked also to the second branch. Due to the wavenumber-preserving transformation, the output frequency content of the first branch has a wider spectrum when compared to the input, which explains the time compression of that portion of the signal evidenced in Fig. 3(c). In this case, the frequency shift and signal compression are observable but contaminated with energy from other wave modes due to the nonadiabatic-induced scattering.

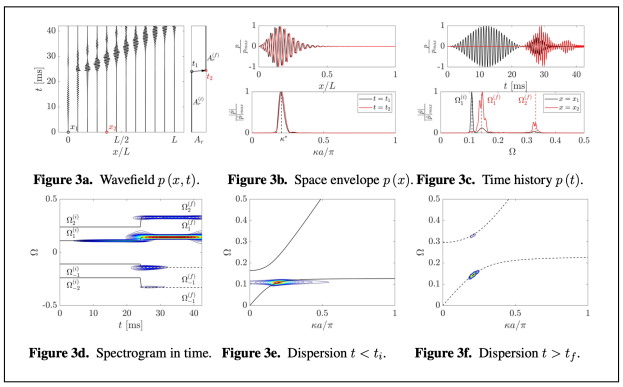

**Figure 3a.** Wavefield $p(x,t)$. **Figure 3b.** Space envelope $p(x)$. **Figure 3c.** Time history $p(t)$.

**Figure 3d.** Spectrogram in time. **Figure 3e.** Dispersion $t < t_i$. **Figure 3f.** Dispersion $t > t_f$.

**Figure 3**. **(A)** Wavefield $p(x,t)$ obtained through a nonadiabatic modulation velocity $v_m^{(1)}$, which is graphically represented in the waterfall plot. In the figure, $x_1$, $x_2$, $t_1$, and $t_2$ are used to mark the space and time coordinates used to produce the plots in Figs. **(B)** and **(C)**. **(B)** Pressure field and corresponding wavenumber content evaluated at constant time instants $t_1$ and $t_2$ before (black curve) and after (red curve) time modulation. The wavenumber is preserved across the time discontinuity. **(C)** Pressure field and corresponding frequency spectrum evaluated at prescribed coordinates $x_1$ and $x_2$. A frequency conversion mechanism takes place, whereby the impinging energy is split over multiple and distinct frequencies. **(D)** Frequency spectrogram evaluated over time. The colored contours represent the energy that is injected to excite $\Omega_1$ and is frequency-converted into different wavemodes $\Omega_j$. The black curves represent the expected evolution of the states in time. **(E-F)** Comparison between dispersion relation and 2D FFTs of the wavefield **(E)** before and **(F)** after time modulation.

A cleaner frequency conversion and signal compression is demonstrated in the second example (ii) corresponding to a modulation velocity $v_m^{(2)} < v_m^{(1)}$, which triggers an adiabatic evolution of the state dictated by the underlying conversion mechanism and described by the black vertical arrow in Fig 2(a). As such, the time history in Fig. 4(a) evidences a single wave packet that transforms with minimal scattering toward other states. This is confirmed by the space snapshot and time evolution of the wave packets reported in Figs. 4(b-c), along with corresponding wavenumber and frequency representations. In absence of further wave modes, Fig. 4(b) illustrates the same wavenumber conservation as in example (i), while 4(c) displays a frequency conversion and compression mechanisms of the impinging wave packet. In addition, the spectrogram in Fig. 4(d) confirms the evolution through the single branch corresponding to $\Omega_1$, while the dispersion plots in Figs. 4(e-f) confirm that the spectral content obeys the predicted behavior of the initial and final states, with no scattering to other wave modes.

The time history relative to the third example (iii) is shown in Fig. 5(a), where now the conversion process is tailored to frequency down-convert the impinging wave and dilate it in time. Such a transformation again follows the arrow in Fig. 2(a), but with a reversed direction. Here, the impinging wave packet is provided with $n = 10$ periods and at a central frequency $\Omega_1^{(i)} = \Omega_1(\kappa^*) = 0.145$, which corresponds to the final frequency $\Omega_1^{(f)}$ of previous examples (i) and (ii). Time modulation is thus performed by bending the dispersion curve and confining the energy content, initially broadband, within a narrower frequency region and with lower propagation velocity. As a result, dilation of the impinging wave packet is observed in Fig 5(c), while 5(b) describes the wavenumber preserving dynamics. Also here, the process with $v_m^{(2)} < v_m^{(1)}$ is considered adiabatic, since a minimal amount of energy is scattered to the other wave modes, as shown in the spectrogram in Fig. 5(d), along with the reciprocal space representation before (Fig. 5)(e) and after (Fig. 5(f)) time modulation.

## 4. CONCLUSIONS

In this paper, we have explored the dynamics of acoustic metamaterials endowed with time-varying Helmholtz resonators. When a sound wave propagates simultaneously to a temporal modulation, the wave packet experiences a frequency conversion dictated by the underlying disper-

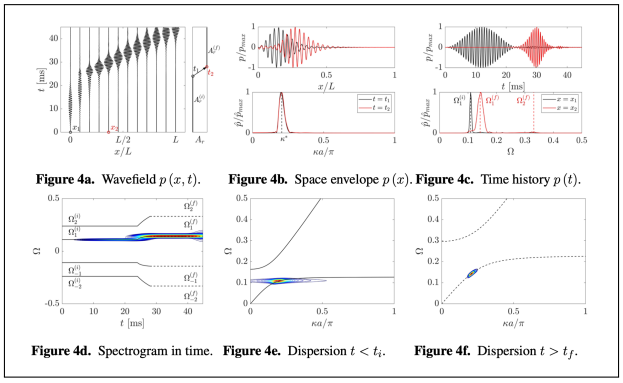

Figure 4a. Wavefield $p(x,t)$. Figure 4b. Space envelope $p(x)$. Figure 4c. Time history $p(t)$.

Figure 4d. Spectrogram in time. Figure 4e. Dispersion $t < t_i$. Figure 4f. Dispersion $t > t_f$.

**Figure 4**. **(A)** Wavefield $p(x,t)$ for an adiabatic transformation driven by a sufficiently slow modulation velocity $v_m^{(2)}$. **(B)** Pressure distribution in space $p(x)$ and corresponding wavenumber content $\hat{p}(\kappa)$ measured before (black curve) and after (red curve) time modulation. **(C)** Pressure distribution in time $p(t)$ and frequency content $\hat{p}(\Omega)$ probed at constant positions $x_1$ and $x_2$. The time domain signal exhibits compression of the wavepacket, which is consistent with a broader spectral content. **(D)** Corresponding frequency spectrogram with superimposed evolution of the underlying wave modes $\Omega_j$. Due to the adiabatic transformation, the energy content does not leak toward the neighboring states and remains located in correspondence of $\Omega_1$. **(E-F)** Comparison between dispersion relation and 2D FFTs of the wavefield **(E)** before and **(F)** after time modulation.

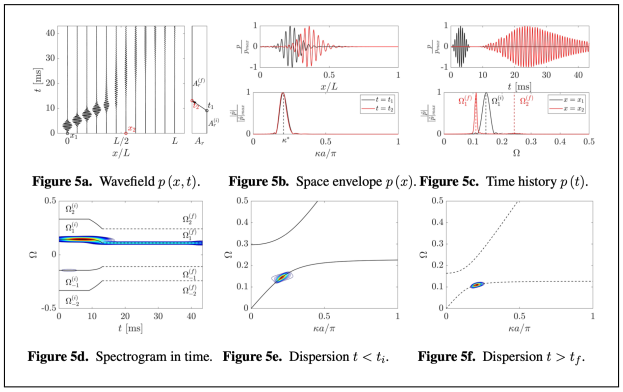

Figure 5a. Wavefield $p(x,t)$. Figure 5b. Space envelope $p(x)$. Figure 5c. Time history $p(t)$.

Figure 5d. Spectrogram in time. Figure 5e. Dispersion $t < t_i$. Figure 5f. Dispersion $t > t_f$.

**Figure 5**. **(A)** Wavefield $p(x,t)$ for a transformation capable of decompressing a wave packet. A sufficiently slow modulation velocity $v_m^{(2)}$ is herein employed to guarantee adiabaticity. **(B)** Pressure distribution in space $p(x)$ and corresponding wavenumber content $\hat{p}(\kappa)$ measured before (black curve) and after (red curve) time modulation. **(C)** Pressure distribution in time $p(t)$ probed at constant positions $x_1$ and $x_2$, along with corresponding frequency content $\hat{p}(\Omega)$. The time domain signal exhibits dilation of the impinging wavepacket, which is consistent with a narrower frequency content. **(D)** Corresponding frequency spectrogram with superimposed evolution of the underlying wave modes $\Omega_j$. The energy content is frequency down-converted and, due to adiabaticity, does not leak toward the neighboring states. **(E-F)** Comparison between dispersion relation and 2D FFTs of the wavefield **(E)** before and **(F)** after time modulation.

sion, which may result in signal compression or dilation. If the speed of the modulation is fast, or nonadiabatic, the time evolution of the wave packet can be accompanied by energy scattering to other wave modes. In contrast, sufficiently slow modulations can frequency transform the impinging wave in an adiabatic manner and without any energy leak to the other dispersion branches. We have established the limiting condition for the modulation speed to distinguish between adiabatic and nonadiabatic processes. The developed framework, illustrated through selected numerical case studies, is generally applicable to a variety of time-varying metamaterial systems. Therefore, the presented results may open new opportunities in time-varying acoustics with application to signal processing, sound isolation, and energy conversion. Future investigations will focus on experimental validation of the concepts herein explored.

## 5. REFERENCES

[1] M. I. Hussein, M. J. Leamy, and M. Ruzzene, "Dynamics of phononic materials and structures: Historical origins, recent progress, and future outlook," *Applied Mechanics Reviews*, vol. 66, no. 4, 2014.

[2] Z. Liu, X. Zhang, Y. Mao, Y. Zhu, Z. Yang, C. T. Chan, and P. Sheng, "Locally resonant sonic materials," *science*, vol. 289, no. 5485, pp. 1734–1736, 2000.

[3] G. Hu, L. Tang, J. Liang, C. Lan, and R. Das, "Acoustic-elastic metamaterials and phononic crystals for energy harvesting: A review," *Smart Materials and Structures*, vol. 30, no. 8, p. 085025, 2021.

[4] H.-W. Dong, S.-D. Zhao, M. Oudich, C. Shen, C. Zhang, L. Cheng, Y.-S. Wang, and D. Fang, "Reflective metasurfaces with multiple elastic mode conversions for broadband underwater sound absorption," *Physical Review Applied*, vol. 17, no. 4, p. 044013, 2022.

[5] G. Ma, M. Xiao, and C. T. Chan, "Topological phases in acoustic and mechanical systems," *Nature Reviews Physics*, vol. 1, no. 4, pp. 281–294, 2019.

[6] R. Süsstrunk and S. D. Huber, "Observation of phononic helical edge states in a mechanical topological insulator," *Science*, vol. 349, no. 6243, pp. 47–50, 2015.

[7] R. K. Pal and M. Ruzzene, "Edge waves in plates with resonators: an elastic analogue of the quantum valley hall effect," *New Journal of Physics*, vol. 19, no. 2, p. 025001, 2017.

[8] K. L. Tsakmakidis, A. D. Boardman, and O. Hess, "'trapped rainbow'storage of light in metamaterials," *Nature*, vol. 450, no. 7168, pp. 397–401, 2007.

[9] J. M. De Ponti, A. Colombi, E. Riva, R. Ardito, F. Braghin, A. Corigliano, and R. V. Craster, "Experimental investigation of amplification, via a mechanical delay-line, in a rainbow-based metamaterial for energy harvesting," *Applied Physics Letters*, vol. 117, no. 14, p. 143902, 2020.

[10] Y. Chen, H. Liu, M. Reilly, H. Bae, and M. Yu, "Enhanced acoustic sensing through wave compression and pressure amplification in anisotropic metamaterials," *Nature communications*, vol. 5, no. 1, p. 5247, 2014.

[11] J. Marconi, E. Riva, M. Di Ronco, G. Cazzulani, F. Braghin, and M. Ruzzene, "Experimental observation of nonreciprocal band gaps in a space-time-modulated beam using a shunted piezoelectric array," *Physical Review Applied*, vol. 13, no. 3, p. 031001, 2020.

[12] I. H. Grinberg, M. Lin, C. Harris, W. A. Benalcazar, C. W. Peterson, T. L. Hughes, and G. Bahl, "Robust temporal pumping in a magneto-mechanical topological insulator," *Nature communications*, vol. 11, no. 1, p. 974, 2020.

[13] V. Pacheco-Peña and N. Engheta, "Temporal aiming," *Light: Science & Applications*, vol. 9, no. 1, p. 129, 2020.

[14] Y. Xia, E. Riva, M. I. Rosa, G. Cazzulani, A. Erturk, F. Braghin, and M. Ruzzene, "Experimental observation of temporal pumping in electromechanical waveguides," *Physical Review Letters*, vol. 126, no. 9, p. 095501, 2021.

[15] J. Santini and E. Riva, "Elastic temporal waveguiding," *New Journal of Physics*, 2022.

[16] L. E. Kinsler, A. R. Frey, A. B. Coppens, and J. V. Sanders, *Fundamentals of acoustics*. John wiley & sons, 2000.

[17] C. Sugino, Y. Xia, S. Leadenham, M. Ruzzene, and A. Erturk, "A general theory for bandgap estimation in locally resonant metastructures," *Journal of Sound and Vibration*, vol. 406, pp. 104–123, 2017.

[18] V. Pacheco-Peña and N. Engheta, "Antireflection temporal coatings," *Optica*, vol. 7, no. 4, pp. 323–331, 2020.

[19] D. J. Griffiths and D. F. Schroeter, *Introduction to quantum mechanics*. Cambridge university press, 2018.

[20] D. Tong, "Quantitative condition is necessary in guaranteeing the validity of the adiabatic approximation," *Physical review letters*, vol. 104, no. 12, p. 120401, 2010.

[21] M. H. Amin, "Consistency of the adiabatic theorem," *Physical review letters*, vol. 102, no. 22, p. 220401, 2009.

[22] S. Ibáñez and J. Muga, "Adiabaticity condition for non-hermitian hamiltonians," *Physical Review A*, vol. 89, no. 3, p. 033403, 2014.